Mon. Not. R. Astron. Soc. **000**, 1–12 (2016) Printed 11 October 2016 (MN LATEX style file v2.2)

Bow-shock Pulsar Wind Nebulae Passing Through Density Discontinuities

Doosoo Yoon[1,2] and Sebastian Heinz[2]
[1]*Shanghai Astronomical Observatory, Chinese Academic of Science, China*
[2]*Department of Astronomy, University of Wisconsin-Madison, Madison, WI, USA*

arXiv:1610.02696v1 [astro-ph.HE] 9 Oct 2016

Accepted 2016 October 6; in original form 2016 June 17

ABSTRACT
Bow-shock pulsar wind nebulae are a subset of pulsar wind nebulae that form when the pulsar has high velocity due to the natal kick during the supernova explosion. The interaction between the relativistic wind from the fast-moving pulsar and the interstellar medium produces a bow-shock and a trail, which are detectable in H_α emission. Among such bow-shock pulsar wind nebulae, the Guitar Nebula stands out for its peculiar morphology, which consists of a prominent bow-shock head and a series of bubbles further behind. We present a scenario in which multiple bubbles can be produced when the pulsar encounters a series of density discontinuities in the ISM. We tested the scenario using 2-D and 3-D hydrodynamic simulations. The shape of the guitar nebula can be reproduced if the pulsar traversed a region of declining low density. We also show that if a pulsar encounters an inclined density discontinuity, it produces an asymmetric bow-shock head, consistent with observations of the bow-shock of the millisecond pulsar J2124-3358.

Key words: pulsars: general – ISM: individual objects: Guitar Nebula – ISM: kinematics and dynamics – stars: winds, outflows

1 INTRODUCTION

Pulsar Wind Nebulae (PWNe) are produced when a pulsar's relativistic wind interacts with the surrounding medium. They produce emission across a broad spectral range from radio synchrotron emission to γ-rays [Gaensler & Slane (2006) and references therein]. A subset of PWNe has been identified in which pulsars with high spatial velocities produce bow-shock structures and cometary shapes [e.g., B1957+20 (Kulkarni & Hester 1988); J0437-4715 (Bell et al. 1995); RXJ1856.5-3754 (van Kerkwijk & Kulkarni 2001); B0740-28 (Jones et al. 2002); J2124-3358 (Gaensler et al. 2002); J1747-2958 (the "mouse" nebula) (Gaensler et al. 2004)]. Such bow-shocks are detectable in collisionally excited H_α emission (van Kerkwijk & Kulkarni 2001; Jones et al. 2002). A theoretical model of Balmer-dominated pulsar bow-shocks was developed by Kulkarni & Hester (1988).

A pulsar's high-spatial velocity is caused by the natal kick of the neutron star during its supernova explosion. Numerous models have been proposed to take into account the deviation from spherical symmetry at the core of the progenitor star. This deviation can occur because of anisotropic neutrino emission during the Kelvin-Helmholtz cooling of the nascent remnant (Sagert & Schaffner-Bielich 2008), anisotropic mass ejection during the SN explosion due to standing-accretion shock instability (Blondin et al. 2003; Hanke et al. 2012), or convective shell-burning during the final life cycle stage of the progenitor star (Burrows & Hayes 1996).

1.1 Young bow-shock nebulae

Bernstein & Hughes (2009) carried out special relativistic, hydrodynamics simulation of pulsar wind bow-shock nebulae, showing that the relativistic backflow from the fast-moving pulsar thermalizes in the form of a slowly inflating, trailing spherical bubble. This energy-driven bubble model also applies to bow-shock nebulae driven by jets from low-mass X-ray Binaries moving through the interstellar medium (ISM) (Yoon et al. 2011).

This model describes the evolution of bow-shock PWNe during the earliest stage, when the pulsar's location is close to its birth-place. The formation of the bow-shock/bubble morphology of bow-shock nebulae is illustrated in the top panel of Figure 1 and can be understood as follows: When a pulsar wind turns on, it inflates an energy-driven bubble, following the well-known solution by Castor et al. (1975), the continuously fed analog to the Sedov-Taylor solution. From simple dimensional arguments it is easy to see that the radius of such a bubble is described by the relation

$$R_{\rm bubble} \sim \left(\frac{\dot{E}\, t^3}{\rho_{\rm ISM}}\right)^{1/5} \quad (1)$$

where $\dot{E}$ is a spin-down loss energy rate, and $\rho_{\rm ISM}$ is an ambient density. The expansion velocity of a wind-driven bubble decreases with time as $v_{\rm b} \propto t^{-2/5}$. Initially, the expansion velocity of this

© 2016 RAS

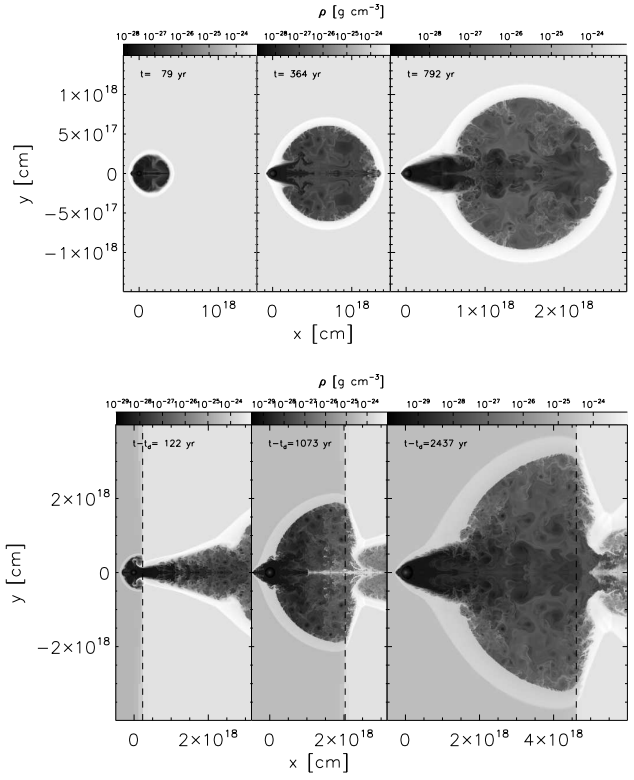

Figure 1. Density slice showing the evolution of expanding pulsar-wind driven bubbles caused by the initial explosion (upper panel) and the passage of a density discontinuity (lower panel). The vertical dashed lines in the lower case indicate the location of the discontinuity. The ambient densities are $\rho_0 = 1.67 \times 10^{-24}\,\mathrm{g\,cm^{-3}}$ (upper case), and $\rho_0 = 1.67 \times 10^{-24} \rightarrow 1.67 \times 10^{-25}\,\mathrm{g\,cm^{-3}}$ (lower case). For both cases, the pulsar is still inside the bubble in left-most plot, breaks out of the bubble in middle plot, and interacts with the ISM producing bow-shock in right most plot.

bubble must therefore be faster than the kick velocity of the pulsar. However, the velocity will eventually drop below the pulsar's velocity, and the pulsar will break out of the bubble. Once this is the case, the pulsar wind will form a classical bow-shock nebula, where, on the up-wind side, the ram pressure of the ISM balances the wind pressure.

As described in Bernstein & Hughes (2009) and Yoon et al. (2011), the bow-shock will have a roughly conical shape behind the pulsar and matter will be accelerated from the high-pressure bow-shock back in the direction of the bubble. The bubble will therefore continue to be inflated while the pulsar moves away from its center.

For young pulsars, one might therefore expect the presence of such a neck/bubble structure in H-alpha images. However, as we will argue, the presence of bubbles behind the pulsar in later stages of pulsar evolution can not be explained by a model in which the bubble is inflated by the initial plerion after the pulsar turned on, given the large distances older pulsars will have traveled through the Galaxy since turning on. These bubbles or cavities are not rare [e.g. PSR J2030+4415, PSR J1509+5850 (Brownsberger & Romani 2014), PSR B2224+65 (Chatterjee & Cordes 2002)]. Observations of bubble- and shell-like structures behind bow-shock PWNe in older pulsars must therefore be explained by a different mechanism.

1.2 The Guitar Nebula

The Guitar Nebula is one of the most spectacular PWNe, produced by one of the fastest known pulsars, PSR B2224+65, which has a transverse velocity of $v_\perp \geq 1000\,\mathrm{km\,s^{-1}}$. In H_α observations, the nebula has a guitar-like shape with a bright head, trailing neck, and a series of roughly circular shells/bubbles (Cordes et al. 1993; Chatterjee & Cordes 2002), shown in Figure 5.

The pulsar most probably originated from the Cygnus OB3 association about 0.8 Myr ago (Tetzlaff et al. 2009), thus the observed bubbles behind it are clearly *not* generated from the pulsar's birth.

From eq. (1), a rapid change in $\dot{R}_{\rm bubble}$ can be brought about by two things:

- A significant, instantaneous increase in the pulsar wind power will generate a new spherical bubble at the location where the wind power increased.
- A sharp decrease in the ISM density ρ will also lead to the inflation of a new bubble.

Time-variable $\dot{E}$ fails to account for the brightening in the constricted region of the Guitar Nebula, and the amount of the variability in $\dot{E}$ is likely negligible compared to large morphological changes of the nebula (Chatterjee & Cordes 2004). Thus, we conclude that variation of the ambient density is likely responsible for the curious morphology of the Guitar Nebula[1]. As an another possible mechanism, Morlino et al. (2015) suggested that mass-loading of encountered neutral hydrogen makes bow-shock unstable likely altering the shock structures and producing the bubbles.

The well-documented multi-phase nature of the ISM supports the notion that bow-shock pulsars will sample a range of densities along their trajectories. For example, small-scale density variations corresponding to tens of AU are observed in the Galactic HI absorption (Deshpande 2000; Faison & Goss 2001). Patat et al. (2010) also detect interstellar medium column density variations on scales of ~ 100 AU, inferred from expansion rates of a Type Ia supernova photospheres.

The question is: Can the morphological details of the Guitar Nebula be explained by a reasonable density structure of the ISM the pulsar is traversing?

The primary goal of this study is therefore to investigate the dynamic evolution of bow-shock PWNe in inhomogeneous environments. Noutsos et al. (2013) reported that the spin-down ages of $\tau_c = P/(2\dot{P})$ and kinematic ages $t_{\rm kyn}$ of a sample of pulsars are within the range $10^5 \sim 10^7$ yr. Under the reasonable assumption that pulsars are born somewhere within 100 pc of the galactic mid-plane, they are expected to intersect the galactic plane at least once in the time travel. It is quite possible that fast-moving pulsars encounter significant changes in their environment.

In this work, using hydrodynamic simulations, we test whether a bubble forms when a pulsar undergoes a sharp change in the ambient density, and examine the temporal evolution of the bubble and the bow-shock after such a change. We also develop an analytic formula for the bow-shock to discuss the morphological variations of the structure of the shock in response to density

[1] It had been suggested that dynamical instabilities in bow-shock backflow could produce similar results (van Kerkwijk & Ingle 2008). As we will show below, our 3-D simulations should capture such instabilities and show no sign of the kind of structure observed in the guitar nebula in the absence of a density discontinuity.

changes in order to provide observational diagnostics for observations of bow-shock PWNe.

We apply this model to the Guitar Nebula, suggesting possible dynamical evolutionary paths. The organization of this paper is as follows. In Section 2, we discuss the numerical method and the initial setup. In Section 3, we discuss the evolution of the PWNe encountering density discontinuities. In Section 4, we compare our numerical results with H_α observations of the Guitar Nebula. We also discuss the effects of an inclined density transition layer to explain the asymmetric bow-shock in PSR J2124-3358. In Section 5, we summarize our results.

2 NUMERICAL METHOD

2.1 The code

Simulations were carried out with the FLASH 3.3 hydrodynamic code (Fryxell et al. 2000), which is a modular and parallel simulation code suitable for solving compressible flow problems. An adaptive mesh refinement (AMR) algorithm in the code enables us to investigate the global evolution of PWNe efficiently using moderate computing resources. The refinement level of the simulations is determined by both the grid position and physical quantity: We set the finest resolution at the pulsar to safely resolve the pulsar wind and the bow-shock structure, which is *lrefine_max*=11 implying that the highest resolution is 1.2×10^{14} cm.

We adopt the piecewise-parabolic solver for our non-relativistic hydro runs (Colella & Woodward 1984). We use a multi-gamma equation of state, where the adiabatic index of the ambient medium is $\gamma_{\rm ambient} = 5/3$ and that of the pulsar wind is $\gamma_{\rm pulsar} = 4/3$. We verified that the (non-relativistic) bow-shock and bubble are well described by our non-relativistic simulations, even though the pulsar wind itself is relativistic, by performing a test study with fully relativistic simulations.

2.2 Implementation of the Pulsar Wind

The bulk of a pulsar's spin-down loss energy is converted into a relativistic pulsar wind (Michel 1969). In general, the wind is likely anisotropic, and the anisotropy of the wind momentum flux should be taken into account to explain detailed bow-shock structures (Vigelius et al. 2007). However, the global features produced by interactions between pulsar winds and the surrounding medium are less influenced by the anisotropy of the wind. Moreover, there is no evidence for an anisotropic or clumped pulsar wind in the series of H_α observations of the Guitar Nebula (Chatterjee & Cordes 2004). Therefore, we approximate the pulsar wind as a spherical inflow, injecting flux isotropically through a spherical surface at the pulsar's location for numerical simplicity (see Section 4).

A pulsar wind is ultra-relativistic, interacting with the ambient medium of either the supernova remnant (SNR) or the ISM, and the Lorentz factor is in the range of $10^4 \sim 10^7$ (Kennel & Coroniti 1984). The pulsar wind produces an expanding bubble of relativistic particles around the neutron star. In principle, to model the *internal* structure and properties of the wind, relativistic and/or magnetohydrodynamic (MHD) simulations are necessary. For instance, Komissarov & Lyubarsky (2004); Del Zanna et al. (2004) studied the evolution of PWNe by using relativistic MHD simulations, and reproduced the polar jet from the pulsar by magnetic hoop stress, which is observed in the X-ray images of Crab Nebula (Weisskopf et al. 2000). Bucciantini et al. (2005) presented the effect of wind magnetization on the evolution of shock layers in bow-shock PWNe, and constraint the flow velocities in the downwind streams. Bernstein & Hughes (2009) focused on studying the inflating bubble behind pulsars by using relativistic hydrodynamic simulations. They concluded that the shockwaves provide the thermalized energy into the bubble, allowing it to expand continuously. However, because the evolution of large-scale bubbles and bow-shock are non-relativistic, we carried out purely non-relativistic hydrodynamic simulations, for reasons of computational feasibility. We compared our results with relativistic pulsar wind model in Bernstein & Hughes (2009), and it shows no noticeable differences in the dynamics of PWNe. To verify that the non-relativistic evolution of the bow-shock and bubble are correctly reproduced by our simulations, we carried out a test run with a fully relativistic algorithm that will be discussed in §4.3.

When a pulsar that loses energy at the rate of $\dot{E}$ moves through an ambient medium with density of ρ_0 at velocity $v_\star$, the wind will generate a bow-shock with the standoff distance R_0, at the stagnation point where the pulsar wind momentum flux is balanced by the ISM's ram pressure:

$$R_0 = \left(\frac{\dot{E}}{4\pi\rho_0 v_\star^2 v_{\rm wind}} \right)^{1/2}, \qquad (2)$$

where the pulsar wind velocity in our case is $v_{\rm wind} = 10^{10}\,{\rm cm\,s^{-1}}$.

The pulsar wind is injected isotropically at a spherical boundary of radius $R_{\rm nozzle}$ centered on the coordinate origin in our grid. We refer to this injection region as the *nozzle*. Because we inject the wind at asymptotic velocity, the injection radius $R_{\rm nozzle}$ of the nozzle is arbitrary, but must be smaller than the standoff distance R_0, which we verified for each simulation.

Values of $\dot{E}$ for the observed pulsar population are in range of $10^{28} \sim 10^{38}\,{\rm ergs\,s^{-1}}$ (Manchester et al. 2005), and pulsars with $\dot{E} \gtrsim 10^{36}\,{\rm ergs\,s^{-1}}$ produce prominent PWNe (Gotthelf 2004). To simulate typical bow-shock PWNe, we set $\dot{E} = 10^{36}\,{\rm ergs\,s^{-1}}$ for all general cases investigated, except for the Guitar nebula model which has a spin-down loss energy rate, $\dot{E} = 10^{33}\,{\rm ergs\,s^{-1}}$ (Chatterjee & Cordes 2004). To resolve the pulsar wind and bow-shock structure appropriately, we set the (adaptive) numerical resolution around the pulsar to have at least 10 cells across $R_{\rm nozzle}$.

2.3 Initial Setup and Boundary Conditions

Rather than simulating a moving pulsar in a stationary medium, we fix the pulsar's location at $x = 0$ for all runs. The external medium is streaming past the pulsar with a fixed velocity $v_{\rm x}$ of 300, 600, or 900 $\rm km\,s^{-1}$ (see Table 1). For the Guitar nebula model, we set the velocity to 1,500 $\rm km\,s^{-1}$. We apply inflow boundary conditions with velocity $v_{\rm x}$ and ISM density and pressure at the lower x-boundary. These velocities represent the actual proper speeds of the pulsars.

Following Cox (2005), the pressure and density in the ambient medium are set to typical values in the galactic disk, $P_0 = 3 \times 10^{-12}\,{\rm erg\,cm^{-3}}$ and $n_{\rm ISM} = 1\,{\rm cm^{-3}}$ for most cases. The ISM temperature is between $10^4 \sim 10^5$ K.

As discussed above, the pulsar produces a spherical bubble in the early stage of the simulation. After a break time, $t_{\rm break}$, the pulsar breaks out of the bubble producing a bow-shock structure. Because the goal of this study is to understand bow-shock evolution when a pulsar propagates through a non-uniform density medium, the density gradient/discontinuity is introduced at the left boundary with varying boundary condition after the bow-shock structure is well developed,$t > t_{\rm break}$, and converged into the analytically expected

shape [eq. (11)]; and it is correctly advected downstream towards the bow-shock.

We examined four configurations of the density change: sharp or secular changes, and either a ten-fold increase or a ten-fold decrease. For all cases, we adopt the same value of distance, $d = 4.12 \times 10^{18}$ cm, between the location of the density discontinuity and initial location for the purpose of comparison. The detailed information we use for this study is listed in Table 1.

It is important to note that the density configurations studied in this work are over-simplifications: The interfaces of real density jumps will not be plane, the transitions may be more or less gradual, and the media on either side of the transition may not be uniform. The goal of this study is to investigate the general behavior of pulsar wind bow shock nebulae in multi-phase gases and to explore the kinds of shapes the shocks can take, and simple density configurations are best suited for providing a robust, simple view of this problem.

Simulations were primarily carried out in axi-symmetry, i.e., 2-D, for the purpose of saving computing resources. We carried out two types of 3-D simulations: one for validating 2-D runs, and a set of 3-D runs for studying the non-axisymmetric case (see Table 1). The latter case investigates a density discontinuity at an angle relative to the pulsar velocity. We investigated two cases: inclination angles of 45° and 5°, respectively, and the result will be discussed at §4.2.

3 RESULTS

3.1 Bow-shock Head

The global evolution of the down-wind shock structure is generally similar to that of supersonic low-mass X-ray binaries (LMXBs) described in Yoon et al. (2011), despite the different engine in the two systems. Around the pulsar, the unperturbed pulsar wind propagates to the termination shock where the wind slows down to subsonic speed because of its interaction with the ambient medium. The bow-shock becomes quasi-conical on the down-stream side (with an opening angle comparable to the Mach angle).

Within the down-wind cone, the shocked pulsar wind propagates away from the pulsar due to the pressure gradient behind the bow-shock. The tail continues to drive the conical down-wind bow-shock as long as its pressure exceeds the thermal pressure in the ambient medium. The bow-shock tail can be described as a narrow (cylindrical) cavity filled with relativistic exhaust from the pulsar.

As discussed in Yoon et al. (2011), the shape of the cavity along the x-axis can be described analytically by using an adiabatic equation of state, the Bernoulli equation, and mass continuity:

$$P_x = a\,\rho_x^{\gamma} \tag{3}$$

$$\frac{1}{2}v_x^2 + \frac{\gamma}{(\gamma-1)}\frac{P_x}{\rho_x} = b \tag{4}$$

$$\pi\, w^2\, \rho_x\, v_x = c, \tag{5}$$

where w is the width of the cavity, and a, b, c are constants. The values of b and c can be expressed in terms of a:

$$b = \frac{\gamma}{\gamma-1} a^{1/\gamma} \left(\rho_0 v_\star^2\right)^{1-1/\gamma}, \tag{6}$$

$$c = \frac{\gamma-1}{\gamma} \dot{E} a^{-1/\gamma} \left(\rho_0 v_\star^2\right)^{1/\gamma-1}. \tag{7}$$

In (Yoon et al. 2011), the value of a was a free parameter due to the complexity in jet geometry, however the spherical shape of pulsar winds allows us to determine a from pressure balance at the standoff position:

$$P_{\rm st,wind} = a\,\rho_{\rm st,wind}^{\gamma} = P_{\rm ram} = \rho_0\, v_\star^2. \tag{8}$$

where $\rho_{\rm st,wind} = \dot{E}/(4\pi R_{\rm st}^2 v_{\rm wind}^3)$ is the wind density at the standoff position. As a result, a can be expressed as

$$a = \frac{\rho_0 v_\star^2}{\rho_{\rm st}^{\gamma}} = \left(\rho_0 v_\star^2\right)^{1-\gamma} v_{\rm wind}^{2\gamma}. \tag{9}$$

Using eqns. (3)-(9), w_1 can be obtained if we assume the pulsar is moving supersonically (*i.e.* $P_x \ll \rho_0 v_\star^2$):

$$w \simeq \left(\frac{1}{2\pi^2}\right)^{1/4} \left(\frac{\gamma-1}{\gamma}\right)^{3/4} \dot{E}^{1/2}\, v_{\rm wind}^{-1/2} \left(\rho_0 v_\star^2\right)^{1/2\gamma-1/2} P_x^{-1/2\gamma} = A\, P_x^{-1/2\gamma}. \tag{10}$$

The pressure can be calculated by the jump conditions for an oblique shock [detailed derivation is included in eqns.(13)-(18) in Yoon et al. (2011)], and the differential equation for the width can be expressed as

$$\frac{dw}{dx} = \left(\frac{\gamma}{2}\right)^{-1/2} \mathcal{M}_0^{-1} \left[\frac{(w/A)^{-2\gamma}}{P_0} - 1\right] \left[\frac{\gamma+1}{P_0}\left(\frac{w}{A}\right)^{-2\gamma} + \gamma - 1\right]^{-1/2}, \tag{11}$$

where P_0 is the ambient pressure and $\mathcal{M}_0 = v_\star/\sqrt{\gamma P_0/\rho_0}$ is the Mach number of the pulsar relative to the ISM.

Integrating eq. (11) yields the analytic shape of the bow-shock and the neck from the physical properties of the pulsar (ambient density, ambient pressure, spin-down loss energy rate, wind velocity, and adiabatic index of the pulsar wind), and is consistent with our numerical results (Figure 2).

This semi-analytic solution is helpful in understanding the morphological evolution of a bow-shock head and a trailing neck when the pulsar moves through a medium in which the density changes gradually. If the ambient density *increases* gradually along the pulsar's trajectory, the ram pressure also increases. Thus, the neck (analytic lines from eq. (11) are plotted in Figure 2) becomes thinner. If the density of the ambient density *decreases*, the bow-shock and the neck become wider. We will apply this analysis to the Guitar Nebula's head in §4.1.1.

3.2 Pulsar wind evolution in density gradients

When the pulsar encounters in increase in the ambient density, the width and opening angle of the neck always decrease, constricting the flow. No new bubble forms in this case, as expected.

3.2.1 Density discontinuities

When the density *decreases*, the width and opening angle of the neck increase. We carried out 2-D hydrodynamic simulations to test if a bubble forms when the pulsar passes through a medium in which the density changes sharply (*i.e.*, density discontinuity). We set the discontinuity to be perpendicular to the pulsar's velocity.

In this case, the standoff distance R_0 increases [eq. (2)] rapidly and the bow-shock becomes wider, producing a bubble at the discontinuity. Figure 1 shows that the formation and the evolution of a bubble proceeds in a similar fashion to the pulsar's initial inflation of a bubble.

In the early stage after encountering the low-density medium, the expansion velocity of the bubble is larger than the pulsar's propagation velocity, thus the pulsar travels inside the expansing bubble. In this case (unlike the initial evolution of a pulsar in uniform

Table 1. Parameter of the Simulations

Model	$v_\star$ [km s^{-1}]	$\dot{E}^a_{36}$	density ratio^b	$R_{\rm nozzle}$ [cm]	transition width ($l_{\rm tr}$)	dimension	incident angle
L10_300	300	1	0.1	1.2×10^{16}	instant	2-D	90°
H10_300	300	1	10	1.2×10^{16}	instant	2-D	90°
L10_600	600	1	0.1	1.2×10^{16}	instant	2-D	90°
L10br_600	600	1	0.1	1.2×10^{16}	5×10^{17} cm	2-D	90°
H10br_600	600	1	10	1.2×10^{16}	5×10^{17} cm	2-D	90°
Uniform_600	600	1	1	1.2×10^{16}	-	2-D	-
L10_900	900	1	0.1	1.2×10^{16}	instant	2-D	90°
H10_900	900	1	10	1.2×10^{16}	instant	2-D	90°
Guitar_LOS90	1500	0.001	three changes^c	5×10^{15}	mixed^d	2-D	90°
Guitar_LOS60	1730	0.001	three changes^c	5×10^{15}	mixed^d	2-D	90°
L10_1000_5deg	1000	1	0.1	5×10^{15}	4.4×10^{16} cm	3-D	5°
L10_1000_45deg	1000	1	0.1	5×10^{15}	instant	3-D	45°

a $\dot{E}_{36} = \dot{E}/(10^{36}\,{\rm ergs\,s^{-1}})$

b Ratio of the final ambient density to the initial density.

c,d There are three changes in the ambient density for our fiducial Guitar nebular model. The ambient density changes to $\rho_{0,\rm init}/5$, further decreases to $\rho_{0,\rm init}/10$, and then finally increases to $\rho_{0,\rm init}$. The first and third changes occur instantly, and the second change occurs smoothly with the transitional length of $1.3\times10^{17}/\sin\theta_{\rm LOS}$ cm, where $\theta_{\rm LOS}$ is the viewing angle between the pulsar's velocity vector and the line of sight.

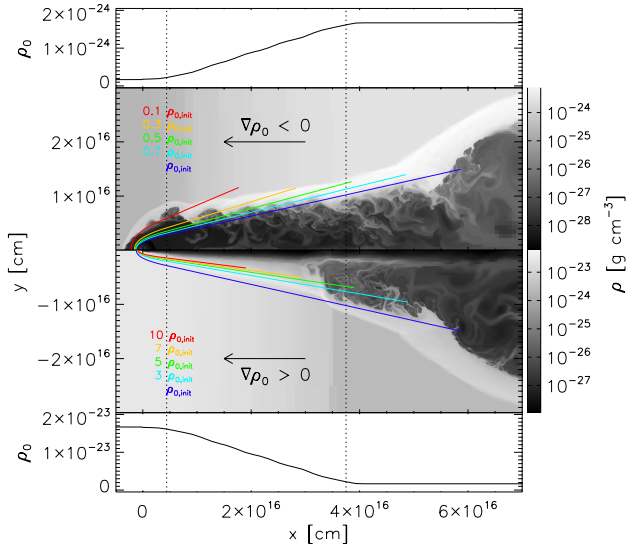

Figure 2. Density slice of the PWN head when a pulsar passes through either 10 fold increase (upper) or 1/10 fold decrease (lower) in ambient density. The top and bottom plots show the smooth variation of the ambient density with a transition width of 5×10^{17} cm (L10br_600 & H10br_600 in Table 1). The transition locations are marked by vertical dashed lines. The colored lines indicate analytic bow-shock solutions with different ambient densities.

medium), the isotropic pulsar wind generates a *hemi-spherical* bubble, since the down-wind half of the pulsar wind is impeded by the high-density medium. The analytic model of the expanding bubble can be applied to the expanding forward-half of the bubble:

$$R_b(t) = \eta^{1/5}\left(\frac{\dot{E}}{\rho_0}\right)^{1/5} t^{3/5}, \tag{12}$$

where η is a constant that equals $125/154\pi$, which is derived by the assumption that the gas is swept-up into a cold, thin shell (Castor et al. 1975).

The expansion velocity slows down with time while the pulsar's velocity is constant, and after a time $t_{\rm break}$, the pulsar breaks out of the bubble, which can be calculated by the bubble radius [eq. (12)] and the pulsar's velocity:

$$t_{\rm break} = \eta^{1/2}\left(\frac{\dot{E}}{\rho_0}\right)^{1/2} v_\star^{-5/2}. \tag{13}$$

at a bubble radius

$$R_{\rm break} = t_{\rm break} v_\star \tag{14}$$

Beyond this point, the pulsar's wind once again generates a bow-shock, a trailing conical neck, and a terminal (hemi-spherical) bubble.

Figure 3 shows a well-developed double-bubble structure behind the bow-shock head. The first bubble originated from the initial launch of the pulsar wind [and is therefore not a result of the density structure of the ambient medium — its position and size will depend on the age and velocity of the pulsar according to eqs. (12) and (14)]; the second bubble is generated when the pulsar encounters the discontinuity.

Note the small "protrusion" on the propagation axis on the right side of the initial bubble. This is a 2-D numerical artifact that is caused by focusing the downstream flows along symmetry-axis (i.e. r=0), impacting the bubble edge. In the 3-D test run, this protrusion disappears. However, given the small volume, the effects of this structure on the evolution of the bubble is negligible.

For comparison, the white cross indicates the location of the pulsar, and the black circles represent the expanding bubbles in the analytic model [eq. (12)].

We carried out simulations with pulsar proper velocities of 300, 600, and 900 km s^{-1}. Figure 4 shows the evolution of the expanding bubbles with time for the different velocity cases. The solid line represents the analytic model in eq. (12), and each filled region represents the location of the shell of the bubble[2] For all cases, the evolving bubbles in the simulations are consistent with the analytic model.

If multiple bubbles are observed in a bow-shock PWN, we

[2] Note that in this work, we neglect cooling, broadening the shell at the surface of the bubble. If cooling is taken into account, the shell thins, but the overall dynamic evolution is not affected (Yoon et al. 2011).

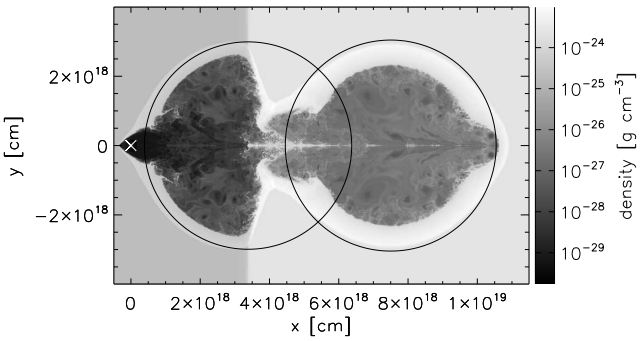

Figure 3. Density contour map when the pulsar penetrates the density discontinuity toward lower ambient density (model L10_600). The black circles are analytic models of the bubbles: the right one is produced by initial explosion and left one is produced when the pulsar encounters the density discontinuity. The white cross indicates the location of the pulsar.

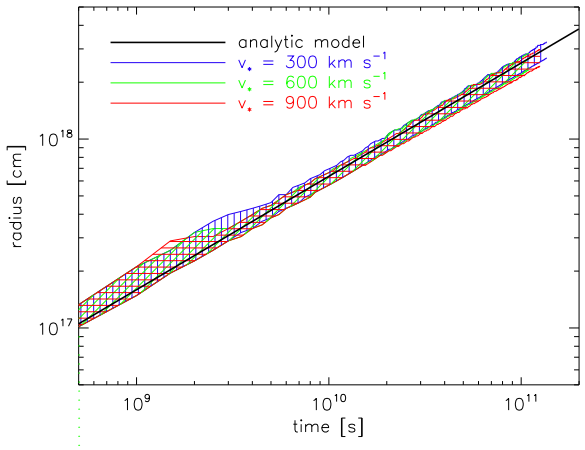

Figure 4. The time evolution of the expanding bubbles. The black solid line represents the analytic solution [eq. (12)], and the colored areas represent the bubble shells between inner and outer radius of the bubble from the simulation results with $v_\star = 300,\ 600,\ 900\,\mathrm{km\,s^{-1}}$.

can constrain the parameters of the density jump from the bubble's geometry. In our simulations, we fixed the separation between the initial position of the pulsar and the density discontinuity to be $l_{sep} = 4.12 \times 10^{18}$ cm. This implies that if the pulsar moves faster, it reached the discontinuity in a shorter time, thereby the size ratio of the second bubble to the first bubble becomes larger compared to the case of slowly moving pulsars. The ratio of the bubble size can be derived from the ratio in eq. (12),

$$R_{b2}(t)/R_{b1}(t) = \left(\frac{\rho_{0,1}}{\rho_{0,2}}\right)^{1/5}\left(1-\frac{t_d}{t}\right)^{3/5} = \left(\frac{\rho_{0,1}}{\rho_{0,2}}\right)^{1/5}\left(1-\frac{l_{\rm sep}}{t\,v_\star}\right)^{3/5}, \quad (15)$$

where $\rho_{0,1}, \rho_{0,2}$ are the ambient densities surrounding the first and second bubble, respectively, and t_d is time when the pulsar encounters the density continuity. The time is related to the separation between the two bubbles by $l_{\rm sep} = t_d \times v_\star$. This robust expression is useful for estimating the density changes in the medium if multiple bubbles are observed.

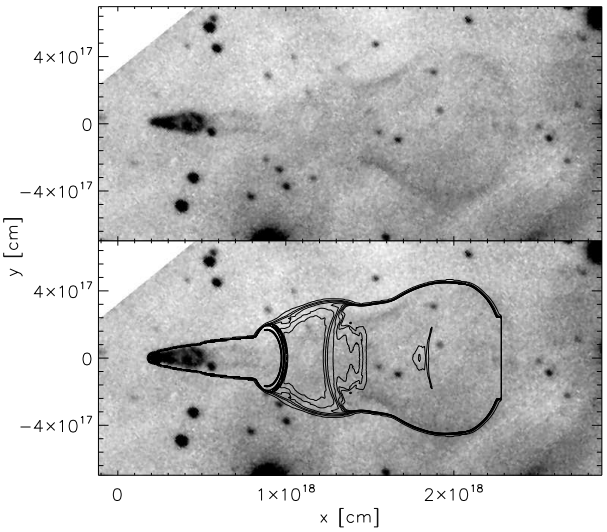

Figure 5. Guitar Nebula in H_α, imaged with the 5m Hale Telescope at Palomar Observatory (Chatterjee & Cordes 2002). In the bottom panel, we overlaid the contour of H_α emission, which is calculated from the numerical results. See §4.1.2.

3.2.2 *Secular changes in density*

We also simulated the case of a pulsar moving through a *smooth* variation of the ambient density, with characteristic transition length Δl over which the density changes, such that

$$\frac{d\rho}{dx} \sim \frac{\rho}{\Delta l} \quad (16)$$

In this case, the morphology of the bow-shock and the neck adjusts smoothly to the changing density, as can be seen in Figure 2.

In this case, a bubble is *not* formed as long as $\Delta l \gg R_{\rm break}$ from eq. (14).

4 DISCUSSION

4.1 Guitar Nebula

The so-called Guitar Nebula is a well known pulsar wind nebula with a curious morphology. The nebula, powered by the relativistic wind from the high-velocity pulsar, PSR B2224+65, displays an H_α bow-shock and multiple shells/bubbles down-stream from the pulsar.

The characteristic spin-down age of the pulsar of 1.1 Myr (Hobbs et al. 2004), and the velocity of $v_{\rm psr} \sim 1500\,\mathrm{km\,s^{-1}}$ imply that its birthplace is very far from its current location, and thus that the two bubble-like structures *cannot* be due to the initial inflation of the pulsar wind. Given the observed parameters of the nebula, we therefore tested whether the effects of a non-uniform density on the dynamical evolution of the nebula can explain the observations.

We adopt the model parameters of the Guitar nebula from van Kerkwijk & Ingle (2008, and references therein): $\dot{E} = 10^{33}\,\mathrm{ergs\,s^{-1}}$, $v_\star = 1.5 \times 10^8\,\mathrm{cm\,s^{-1}}$. The spin-down loss energy of the nebula is a few orders of magnitude lower than that of typical H_α bow-shock PWNe (Gotthelf 2004). However, the extremely fast motion of the pulsar in the Guitar nebula and the likely low density of the environment enables PSR B2224+65 to produce the visible bow-shock features despite of such low $\dot{E}$.

The pulsar is located slightly out of the galactic plane

($l = 108.6°, b = 6.8°$) (Cordes et al. 1993), indicating that it is about 227 pc away from the plane if we assume the distance of 1.8 kpc, estimated from the pulsar's dispersion measure of DM= $35.3\,\mathrm{pc\,cm^{-3}}$ and the NE2001 electron density model (Cordes et al. 1993; Cordes & Lazio 2002; van Kerkwijk & Ingle 2008). Hence, we adjust the ambient density and pressure in the Guitar Nebula model from Galactic mid-plane values, which drop to $1.2\times10^{-25}\,\mathrm{g\,cm^{-3}}$ and $1.7\times10^{-12}\,\mathrm{dyne\,cm^{-2}}$, respectively (Cox 2005). Note that since the ionized material along the line of sight likely biases the DM upward, the distance may be over-estimated (Chatterjee & Cordes 2004).

4.1.1 *Bow-shock and neck*

Chatterjee & Cordes (2004) observed morphological changes of the Guitar Nebula's head in H_α emission between two epochs spaced 7 years apart (1994, 2001). Under the assumption of a momentum-conserving bow-shock model (Wilkin 1996), they modeled the shock front, concluding that the ambient density at the nebula tip should decrease by $n_{\rm A}(2001)/n_{\rm A}(1994)\approx 0.7$, where $n_{\rm A}$ is the number density of the surrounding medium. However, this work is purely analytic.

To test this conclusion, we carried out numerical simulations to understand how bow-shock and trailing neck evolve if the pulsar moves through the medium with either gradual increase or decrease in the ambient density. As discussed in §3.2.2, Figure 2 shows that if the pulsar moves through a medium with decreasing density (*i.e.*, $\nabla\rho_0<0$), the standoff radius becomes larger, and the shape of bow-shock becomes rounder, producing a wider neck.

On the other hand, if the pulsar moves through a medium with increasing density (*i.e.*, $\nabla\rho_0>0$), the stagnation point/standoff distance moves closer to the pulsar, and the neck becomes thinner than in the initial density medium. The analytic lines in the figure describe the change of in the shape of the shock fronts along the density variation in the medium.

Figure 6 shows that the morphology of the bow-shock and neck differs between the three cases: $\nabla\rho_0<0$, $\nabla\rho_0>0$, and constant ρ_0. We found that the rounder shape in the tip of the bow-shock head and the flattened neck in case of $\nabla\rho_0<0$ is in good agreement with observed morphology of the Guitar head at 2001 [See Figure 2 in (Chatterjee & Cordes 2004)], indicating that the pulsar likely moves decreased-density medium during the epochs.

Under the assumption of constant spin-down loss rate $\dot{E}$, spatial velocity, and pulsar wind velocity, we can obtain the density ratio in the medium by using eq. (2), into which we plug the ratio of standoff data, $\theta_{0,2001}/\theta_{0,1994}\approx 1.25$, where θ_0 is a modeled standoff angle (Chatterjee & Cordes 2004). The resultant density ratio, $\rho_{0,2001}/\rho_{0,1994}$, is 0.64 which is consistent with Chatterjee & Cordes (2004).

4.1.2 *Guitar Body*

The origin of the bubbles behind the pulsar in the Guitar Nebula has been elusive because the pulsar is far away from its birth place, the Cygnus OB3 association (Tetzlaff et al. 2009), so the initial explosion cannot be responsible. However, as we discussed in § 3.2, an expanding bubble can be produced if the pulsar encounters a density discontinuity at which the density sharply decrease.

We adopt the angular separation and angular size of the bubbles that were reported by van Kerkwijk & Ingle (2008). We assumed a distance of $d = 1.8\,\mathrm{kpc}$. The separation length from the pulsar to the first and second bubbles (named in order of decreasing distance from the pulsar) can then be calculated as $l_{\rm b1} = 1.75\times10^{18}$ cm and $l_{\rm b2} = 1.1\times10^{18}$ cm, respectively. Given the pulsar proper velocity, $v_\star = 1.5\times10^8\,\mathrm{cm\,s^{-1}}$, we expect that the first and second bubbles were born 370 and 233 years ago, respectively, while the pulsar passes through a non-uniform density medium.

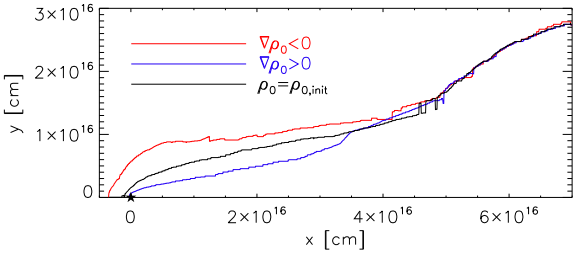

Figure 6. Comparison of the observed shape of the bow-shock head of the guitar nebula with simulation results. The red, blue and black represent the bow-shock and the trailing neck from the model of L10br_600, H10br_600, and Uniform_600, respectively. The black star symbol indicates the location of the pulsar.

Suppose that each bubble is produced when the pulsar passes through a density discontinuity. Then, in order to reproduce multiple bubbles in the Guitar Nebula, we can calculate the change of ambient density required to explain the bubbles. Using the energy-driven bubble model [eq. (12)], the ratio of the ambient density around the second bubble (ρ_2) and first bubble (ρ_1) can be expressed as,

$$\frac{\rho_2}{\rho_1}=\left(\frac{R_{\rm b1}}{R_{\rm b2}}\right)^5\left(\frac{l_{\rm b2}}{l_{\rm b1}}\right)^3, \qquad (17)$$

where R is the bubble radius.

Given the parameters for the two bubbles in the guitar nebula (van Kerkwijk & Ingle 2008), the ratio of the bubble radius is $R_{\rm b1}/R_{\rm b2} = 16''/9'' \approx 1.78$, and the ratio of the separation is $l_{\rm b1}/l_{\rm b2} = 65''/41'' \approx 1.58$. This implies that the density around the second bubble should be 4.5 times *higher* than that around the first bubble. Since a higher density medium in the pulsar's path does not produce a bubble, the presence of the second (smaller) bubble cannot be explained without another region of even higher density between the two media (i.e., a thin wall) with density higher than ρ_2.

Such a complicated density structure would require a significant level of fine-tuning. Furthermore, in this model, the H_α emission in the second bubble should be brighter than that in the first bubble due to the enhanced ambient density. This is inconsistent with the observed features, at which the H_α emission of the second bubble-like structure is a factor of 5 dimmer than that of the first bubble (Chatterjee & Cordes 2002).

Based on the intuition gained from the simulations presented above, we propose the following scenario for producing the guitar shape of the nebula as the result of the pulsar traversing a region of low and decreasing density before re-entering a higher density region: (1) The first (larger) bubble is produced when the pulsar passes through a low density discontinuity. (2) The second bubble is produced as the pulsar moves along the decreasing density gradient. (3) The neck requires passage into a region of higher density.

We carried out two sets of 2-D hydrodynamic simulation to test this scenario to reproduce the aspect ratio of the guitar for two different viewing angles, (model Guitar_LOS90 seen edge-on, and

Guitar_LOS60 seen at 60°). The ambient density variation is shown in the upper plot of Figure 7. The density contour map in Figure 7 shows that this model reproduces the shape of the guitar body and the narrow neck with reasonable precision.

In order to compare this result to observed H_α emission, under the assumption of collisional ionization equilibrium, we calculated the emission from the numerical result. Note that we generated 3-D data based on the 2-D axi-symmetric results to obtain the projected H_α emission.

The ionization balance in the shocked gas was calculated by the MAPPING III code (Sutherland & Dopita 1993). The temperature of the shocked shell is above 10^6 K, thus the gas is nearly fully ionized. The right panel of Figure 7 shows the surface brightness in H_α for the model. The surface brightness around the rim of the bubble is about 10^{-5} photons cm^{-2} s^{-1} arcsec^{-2}, which is consistent with the H_α observation (van Kerkwijk & Ingle 2008).

The H_α emission of the inflated structure between the bubble and the pulsar is a factor of 7 dimmer than that of the rim of the bubble due to the low density in the medium, which is consistent with the observation.

Note that the bright emission far down-stream beyond the bubbles (on the fourth dashed line on the right-hand-side of the image) does not have a corresponding feature in the observed map. However, given that we cannot constrain the ratio of the density in this region of the flow other than saying that it must be higher than in region (b), since no observed features have been identified in this region of the flow, the simulation should not be expected to reproduce the results.

The bubble is flattened toward the discontinuity because the high density suppresses the expansion of the bubble in this region. However, its shape can project into a circle if the viewing angle, $\theta_{\rm LOS}$, between the pulsar velocity vector and the line of sight (LOS) varies (see right panel of Figure 7). Although $\theta_{\rm LOS} \sim 90^\circ$ is preferred because otherwise the three-dimensional velocity of the pulsar can be extremely high, the viewing angle is not well constrained between $30^\circ - 60^\circ$ (Chatterjee & Cordes 2002, 2004). In the model Guitar_LOS60, we set the pulsar's velocity of $v_\star = 1.5 \times 10^8 / \sin 60^\circ$ cm s^{-1}, and the location of the density variation from the pulsar to be farther away by $1/\sin 60^\circ$. We rotated the data with the viewing angle of $\theta_{\rm LOS} = 60^\circ$, and the projected H_α surface brightness shows the round shape of the bubble which provides a better match to the observed shape. We overlaid the contour of the simulated surface brightness on the observed H_α image, which is in good agreement with the observed shape (bottom panel of Figure 5)

The ambient density around the bubble was set using eq. (12) and the observed properties of the pulsar wind and bubble:

$$\rho_0 = \frac{\eta \dot{E}\, t^3}{R_b(t)^5} = \frac{\eta \dot{E}\, \Theta_{l,\perp}^3}{\Theta_b^5 \mu_{\star,\perp}^3 d^5} \simeq 2.5 \times 10^{-26}\,{\rm g\,cm^{-3}}, \quad (18)$$

where, $\Theta_{l,\perp}$ is the angular separation between the bubble center and the pulsar, and Θ_b is the angular radius of the bubble, and $\mu_{\star,\perp}$ is the transverse angular velocity of the pulsar. The angular velocity is estimated to $\mu_{\star,\perp} \simeq 182 \pm 3$ mas yr^{-1} (Harrison et al. 1993). The resulting hydrogen number density can be calculated from the density above to $n_{\rm H} \simeq 0.01$, which is consistent with the nominal ambient density of the nebula, reported by Chatterjee & Cordes (2002).

Since the ISM exists in multiple phases depending both in temperature and chemical composition (Draine 2011), accurately representing the density structure around the pulsar would require an unreasonable degree of fine-tuning and carry a large amount of uncertainty. The chosen density structure in the simulations (plane parallel with simple uniform regions) is clearly an over-simplification. However, given the multi-phase nature of the ISM it is reasonable that the pulsar will transverse density inhomogeneities of scale similar to the size of the guitar (roughly of order a parsec). For example, a cluster of stellar winds could generate a local underdensity in the medium that would correspond to the simulated density structure to lowest order.

Given the uncertainties in the observed physical quantities, eq. (18), we can estimate the uncertainty of the density to be $\sigma_{\rm rho} \sim 130\%\,\rho_0$. The dominant factor determining the uncertainty in the density is the distance, d: the distance is obtained from the pulsar dispersion measure considering a model of the Galactic electron density (Taylor & Cordes 1993), and it is constrained to within roughly 25% uncertainty to be $d = 2 \pm 0.5$ kpc(Chatterjee & Cordes 2002). The structure of the density discontinuity is unconstrained on scales significantly later than the guitar body size.

In the simulation, we set three different ambient densities along the pulsar's path to establish the observed structures: thin neck, middle bubble-like structure, and the right-most expanding bubble (see Figure 7). The corresponding density ratio of each region is $(\rho_{0,1}, \rho_{0,2}, \rho_{0,3}) = (5, 0.5, 1)\rho_{0,3}$, where the subscripts represent each region from left to right and $\rho_{0,3} = 2.5 \times 10^{-26}$ g cm^{-3} [eq. (18)]. Considering the error in the distance, the uncertainties of the density ratio are estimated to be $\sigma_{\rho_{0,1}/\rho_{0,3}} \sim 8\%\,\rho_{0,1}/\rho_{0,3}$ and $\sigma_{\rho_{0,2}/\rho_{0,3}} \sim 70\%\,\rho_{0,2}/\rho_{0,3}$, respectively.

4.2 Asymmetric Shape of Bow-shock

The H_α-emitting bow-shock nebula powered by the nearby millisecond pulsar J2124-3358 has a highly asymmetric shape in its head around the pulsar's velocity vector (Figure 8). Assuming that the velocity vector of the pulsar is perpendicular to the line of sight, the standoff angle is estimated to $2''.6$, implying that the standoff distance is $R_0 \approx 3.4 \times 10^{-3}$ pc with the distance of $\approx 270\,pc$ (Cordes & Lazio 2002). The upper bow-shock is about 3.5 times wider than the lower bow-shock, and the upper one has a broader shape. The origin of the asymmetry has been elusive and cannot be explained by the interaction of an isotropic pulsar wind with a homogeneous ambient medium. More interestingly, a kink-like shape, which is a factor of 2 brighter than the nebula average, appears in the lower bow-shock (denoted by "K" in Figure 8).

One possible reason for the asymmetry in the bow-shock is that the density in the region to the North of the pulsar is lower than in the South, with the pulsar currently crossing a density discontinuity that is inclined with respect to the pulsars velocity vector (different from the geometry discussed so far). If we assume that the asymmetry in PSR J2124-3358 is caused by the differences in ambient density between the Northern and the Southern side, we can estimate the relative densities from by-eye fits of analytic bow-shock models for different densities; five such models are overlaid on the observed bow-shock (right panel of Figure 8). For the analytic lines, we adopted the pulsar's spin-down loss energy of $\dot{E} = 4.3 \times 10^{33}$ ergs s^{-1} (Toscano et al. 1999) and the projected space velocity of 60 km s^{-1} (Gaensler et al. 2002).

This suggest that the ambient medium of the upper region may be approximately 40 times less dense than that of the lower region, unless there is bulk motion of the ambient gas to decrease the angle of the lower bow-shock. The upper half of the bow-shock deviates from a simple analytic model farther back along the flow (denoted by a yellow circle in the figure). The analytic lines converge to become parallel to the pulsar's velocity vector after $x = 2 \times 10^{17}$ cm, because the momentum flux of the ISM pushes the bow-shock backward due to the pulsar's proper motion. However, the observed

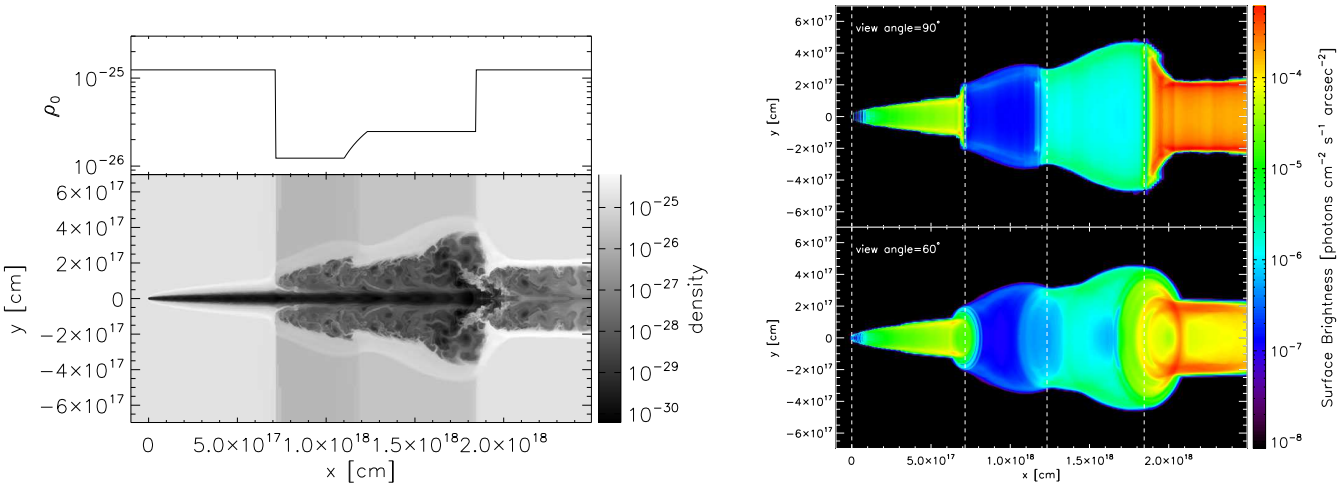

Figure 7. Left panel:Density contour map for the Guitar Nebula model (model Guitar_LOS90). The variation of ambient density was described in upper plot. Right panel: Projected H_α emissions in logarithmic scale with the viewing angle of 90°(upper) from the model Guitar_LOS90 and 60°(lower) from the model Guitar_LOS60. The left most vertical dashed line indicates the pulsar's position and other vertical lines indicate the locations of density change in the medium.

bow-shock has an opening angle of 30° (cyan dashed line in Figure 8). This deviation may be caused by an overestimate in the distance to the pulsar and/or the uncertainty in the viewing angle of the bow-shock, i.e., the angle between the velocity vector and the line of sight: if the distance is shorter than estimated, the bow-shock of downstream likely retains a larger opening angle in two reasons. First, in the case of a shorter distance (i.e. smaller physical size of the observed structure), the bow-shock may not reach the region where it becomes parallel to the pulsar's proper motion. Second, the pulsar's velocity should be lower than the estimated one, implying that the opening angle of the bow-shock is likely wider than what we can see from the analytic lines in the figure.

Alternatively, this mismatch may be produced by the formation of flow instabilities as the pulsar passes the density gradient. This will be discussed in detail below.

Gaensler et al. (2002) argued that the asymmetric bow-shock structure is caused by the combination of three components: a density gradient in the ISM, a bulk flow in the ambient medium, and an anisotropy in the pulsar wind. However, in their semi-analytic models for the structure, an inclination angle between the pulsar's velocity vector and the density discontinuity cannot be taken into consideration due to the complexity. In the models, the density gradient was either perpendicular or parallel.

To study the effect of the inclination angle φ of the density discontinuity relative to the proper motion of the pulsar, we carried out a 3-D hydrodynamic simulation of a bow-shock PWN in which the pulsar moves into a lower-density medium such that its velocity vector is inclined with respect to the transition layer at an angle of $\varphi = 5°$.

This angle is chosen somewhat arbitrarily, but is set to be small enough to reproduce bow-shock structures that are distinct between the shock generated at the low ambient density the pulsar is propagating into and the shock generated at the initial, higher ambient density in the medium the pulsar is initially traveling through. If the angle is larger than the opening angle of the bow-shock in the low-density medium (cyan dashed line in the right panel of Figure 8), the shape of the bow-shock will become more symmetric. The rather complicated shape of bow-shock in the PSR J2124-3358 (e.g., the presence of two kink-like structures; see Figure 8) requires a small inclination angle. The generation of the complicated structures will be discussed in detail below.

Unlike the semi-analytic model in Gaensler et al. (2002), our model focuses only on the variation of the ambient density along the pulsar's passage without taking any anisotropy in the pulsar wind into consideration.

An accurate to-scale 3-D simulation of the J2124-3358 bow-shock would require an unreasonable amount of computing time for the bow-shock to establish, given the small Courant time step imposed by the pulsar wind velocity. For computational expedience, we thus approximated the system using a non-relativistic 3-D model similar to the other models used in this paper, the parameters of which are given in Table 1 (L10_1000_5deg). The primary aim of the simulations is to explore whether the asymmetry of pulsar wind bow-shocks can be produced by simple inhomogeneities in the environment.

In our numerical model, the ambient density decreases to 1/10 of the initial density ρ_0 across a transition zone, with a smooth density transition over a length scale $\Delta l_{\rm tr}$, such that the pulsar encounters a projected transition length scale

$$\Delta l_{\rm tr,x} = \Delta l_{\rm tr}/\cos(5°) = 5 \times 10^{17}{\rm cm} \quad (19)$$

in the direction of motion, i.e., the x-direction, which is 100 times larger than the standoff distance of the pulsar wind.

The transition length is crucial for determining how rapidly the bow-shock expands while the density is changing. If the transition length is small compared to standoff distance (i.e., $\Delta R_0/\Delta l_{\rm tr,x} \gg 1$), as discussed in §3.2, the tip of the bow-shock head inflates in a short time, producing an expanding bubble-like structure behind the pulsar.

However, if the transition length is sufficiently large, the evolution of the bow-shock head and trail is smooth without bubble formation because the radius of curvature of the bow-shock head increases and the trail becomes flat (see §4.1.1).

Figure 9 shows the temporal evolution of the density while the pulsar moves into the low density medium. The transition area is marked with a red dot-dashed line, and the white cross represents the pulsar (bottom right panel). The magenta lines are the analytic

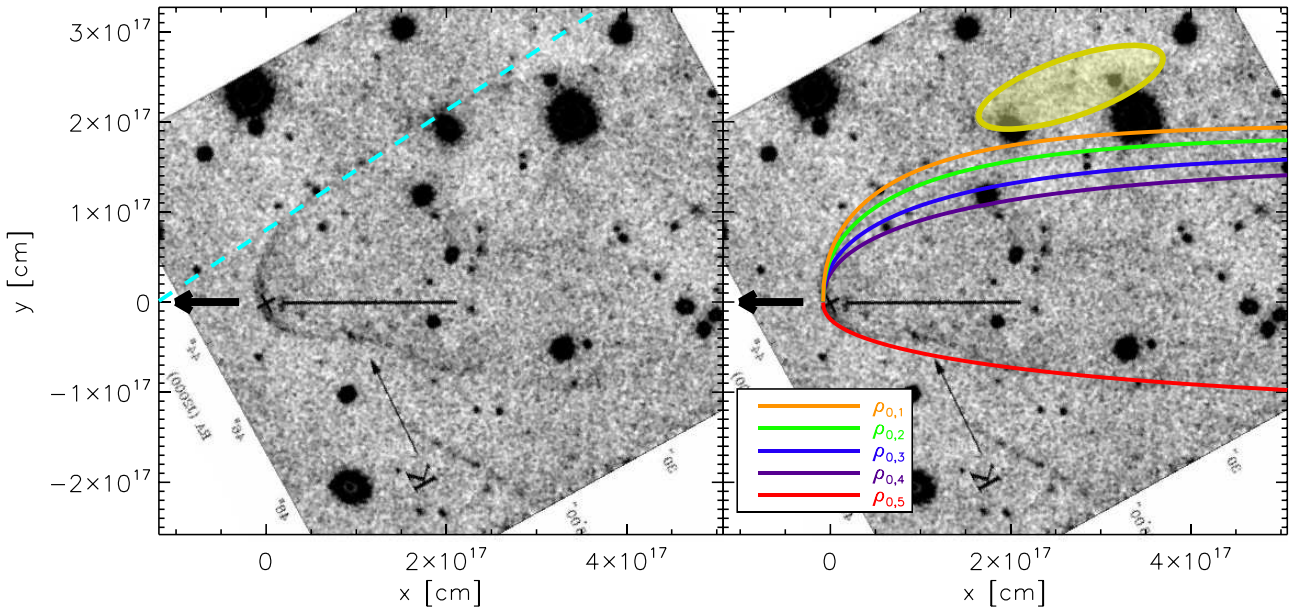

Figure 8. H_α image of PSR J2124-3358 (Gaensler et al. 2002). In the left panel, the cyan dashed line represents the maximum opening angle of the bow-shock, which is $\sim 30°$. In the right panel, we overlaid the analytic bow-shock lines with several ambient densities on the image: $\rho_{0,1} = 2.5 \times 10^{-25}$ cm, $\rho_{0,2} = 4.2 \times 10^{-25}$ cm, $\rho_{0,3} = 9.2 \times 10^{-25}$ cm, $\rho_{0,4} = 1.7 \times 10^{-24}$ cm, $\rho_{0,5} = 1 \times 10^{-23}$ cm. The yellow circle represents the area where the analytic line deviates from the observed bow-shock.

solutions for the bow-shock in uniform medium with ambient density ρ_0 (lower line) and with 1/10 ρ_0 (upper line), respectively.

At early stages of the simulation, the bow-shock is symmetric. However, as expected, it becomes asymmetric after the pulsar moves into the low density medium; the width of the neck w, and the asymptotic bow-shock angle, dw/dx, are inversely-proportional to the ambient density. We ignore the evolution of the initial bubble, since it is unrelated to the crossing of the density discontinuity (it is formed as the pulsar turns on at the start of the simulation, as discussed above), and only focus on the properties of the bow-shock. We note that in the yellow area, the bow-shock shows a deformation that deviates somewhat from the analytic line. This is because although the transition length $\Delta l_{\rm tr,x}$ is long enough to avoid the generation of an expanding bubble, the sudden change of stand-off distance shortly makes the shock unstable while the pulsar is passing the transition zone. It is plausible that the kink-like structure observed in the bow-shock of J2124-3358 is produced by a similar instability at the intersection between the bow-shock and the transition layer.

For comparison, we also performed a simulation with the larger inclination angle of $\varphi = 45°$ and a transition length of $\Delta l_{\rm tr,x} = 0$. Figure 10 shows the time evolution of the density map in this case. As we discussed above, the zero transition layer (or, $\Delta l_{\rm tr,x} \ll R_0$) results in the production of expanding bubble rather than the smooth change of bow-shock morphology. In this case, the asymmetric feature appears only when the pulsar is in the bubble: After the pulsar breaks out of the bubble, it recedes from the transition layer, producing a symmetric bow-shock. However, the round shape of the bubble is not consistent with the overall shock morphology of J2124-3358, although a kink-like structure appears at the intersection between the lower bow-shock and the transition layer (denoted by "K" in the figure).

4.3 Validation of the non-relativistic approximation

Pulsar winds are magnetized and relativistic outflows, indicating that relativistic magnetohydrodynamic (MHD) treatment is required in studying the *internal* flow structure and the emission properties of bow-shock PWNe (Bernstein & Hughes 2009). However, even for the fastest known pulsar, the pulsar velocity $v_\star$ is of 2 orders of magnitude less than the speed of light, and the expansion velocity of the bubble and neck are correspondingly smaller, which is manifestly non-relativistic.

We carried out some subsets of runs with the FLASH special relativistic hydrodynamic (RHD) solver to compare with our results with non-relativistic hydrodynamic simulations. In these test runs, we varied the velocity of the pulsar wind ($v_{\rm wind} = 0.33c$, $0.6c$, $0.9c$, $0.99c$) for both non-relativistic and relativistic runs, and otherwise we used identical parameters.

Figure 11 shows the evolution of pulsar-wind-inflated bubbles. For various pulsar wind velocities, the trends of the bubble expansion are consistent with the analytic solution (red solid line) from eq. (12). The error is about 8% for the extreme case ($v_{\rm wind} = 0.99c$), and is less then 2% for rest of the cases, validating our assumption that relativistic corrections are moderate.

A fully relativistic MHD treatment is beyond the scope in this study. As we discussed, the relativistic effect is negligible in the evolution of bubbles. As argues by Bucciantini et al. (2005), the variation of a pulsar wind magnetization does not change the properties of the *external* shock significantly, apart perhaps from the very head of the nebula. Future simulations in full MHD should verify this assumption.

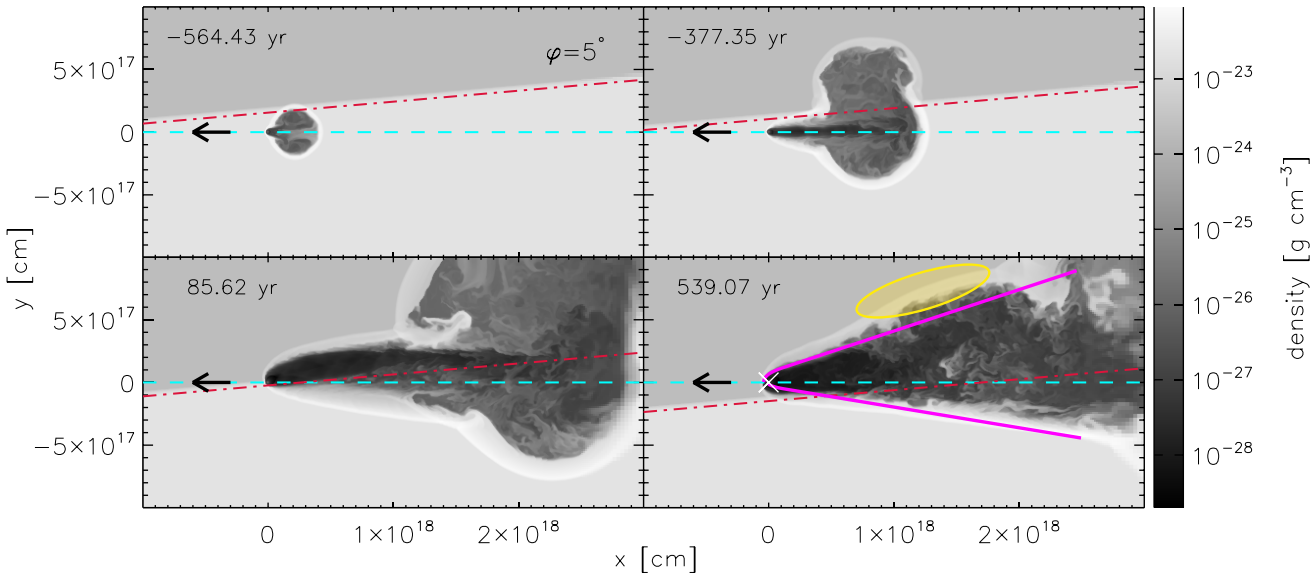

Figure 9. Density slices of the temporal evolution as the pulsar traverses a decrease in the density of the external medium which has an inclination angle of 5° with respect to the pulsar's velocity vector (black arrow). The ambient density decreases to $1/10\rho_0$ with a transition length of $\Delta l_{\rm tr,x} = 100R_0$, where R_0 is the standoff distance of the pulsar wind [see eq. (2)]. The bottom left panel shows the density map when the pulsar is within the transition layer. In the bottom right panel, the pulsar passed the layer, and the bow-shock has re-shaped. The white cross indicates the location of the pulsar, and the cyan dashed line and red dot dashed line represent the pulsar's trajectory and the surface of density change, respectively. The magenta lines represent the analytic bow-shock [eq. (11)], in which the upper line is calculated for a decreased ambient density of $1/10\rho_0$ and the bottom line is calculated for the initial ambient density ρ_0. The yellow area marks the region where the bow-shock deviates from the analytic solution.

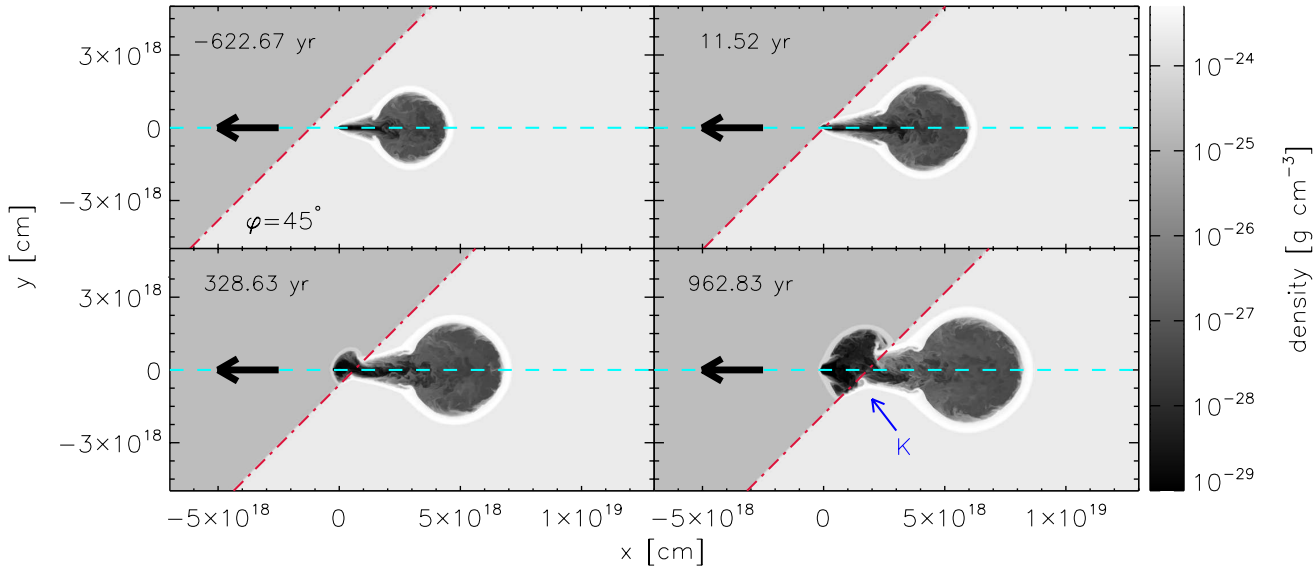

Figure 10. Temporal evolution of the density maps as the pulsar traverses a density decreased medium, which has the inclination angle of 45° to the velocity vector. The transition length is $\Delta l_{\rm tr,x} = 0$. The rest configuration is same with the model in Figure 9.

5 CONCLUSION

In order to study the effect of inhomogeneous environments on the structure of bow-shock PWNe, we performed a series of 2-D and 3-D hydrodynamic simulations.

We confirm the expectation that if a pulsar passes through a decreasing density gradient in the medium, the standoff distance and radius of curvature of the bow-shock increase. As a result, the overall shape of the trailing neck becomes more flattened during the transition. Conversely, if the density in the medium is increasing, the radius of curvature and standoff distance of the bow-shock decrease. We derived analytic formula for the shape of the bow-shock head and the trailing neck as a function of ambient density and pulsar wind parameters.

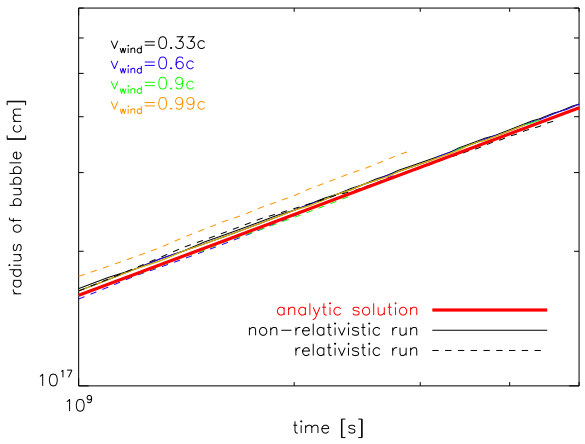

Figure 11. Results from the validation simulations of pulsar wind simulations. Shown is the time evolution of the radius of the expanding pulsar wind driven bubbles. The red solid line represents the analytic bubble solution [eq. (12)], and other colored lines represent the inner radius of the bubbles from the simulation results with $v_{\rm wind}$ = 0.33c, 0.6c, 0.9c, 0.99c. The solid lines are non-relativistic hydrodynamic results, and the dashed lines are relativistic hydrodynamic results, showing that the scaling solution is in excellent agreement with the simulations and that relativistic corrections to the solutions are moderate.

We applied this analysis to the head and bow-shock of the Guitar Nebula, and suggest that the pulsar in the nebula is currently moving through a density-decrease.

If a pulsar encounters a density discontinuity at which the density decreases, the standoff distance increases rapidly, producing a hemispherical bubble bounded by the high-density medium. Eventually, the pulsar will break out of the bubble at radius $R_{\rm break}$, generating a characteristic neck-bubble structure. We showed that the condition for bubble-formation is that the transition length Δl is smaller than the break-out radius $R_{\rm break}$.

We can reproduce the observed shape of the Guitar Nebula from a series of density changes in the medium which suggests that the pulsar traversed a lower density region that gave rise to the body of the guitar nebula. Projection effects of the hemispherical bubble can explain the round appearance of the body of the guitar nebula.

We showed that when the density discontinuity is inclined to the pulsar's velocity vector, it generates an asymmetry in the shape of the bow-shock head, potentially explaining the observed asymmetry in the bow-shock of PSR J2124-3358.

ACKNOWLEDGMENTS

We would like to thank Bryan Gaensler, Enrico Ramirez-Ruiz, and Brian Morsony for helpful discussions. SH and DY acknowledge support form NSF grant AST 0908690.

REFERENCES

Bell J. F., Bailes M., Manchester R. N., Weisberg J. M., Lyne A. G., 1995, ApJ, 440, L81
Bernstein J. P., Hughes P. A., 2009, Journal of Computational Physics, 228, 6212
Blondin J. M., Mezzacappa A., DeMarino C., 2003, ApJ, 584, 971
Brownsberger S., Romani R. W., 2014, ApJ, 784, 154
Bucciantini N., Amato E., Del Zanna L., 2005, A&A, 434, 189
Burrows A., Hayes J., 1996, Physical Review Letters, 76, 352
Castor J., McCray R., Weaver R., 1975, ApJ, 200, L107
Chatterjee S., Cordes J. M., 2002, ApJ, 575, 407
—, 2004, ApJ, 600, L51
Colella P., Woodward P. R., 1984, Journal of Computational Physics, 54, 174
Cordes J. M., Lazio T. J. W., 2002, ArXiv Astrophysics e-prints
Cordes J. M., Romani R. W., Lundgren S. C., 1993, Nature, 362, 133
Cox D. P., 2005, ARA&A, 43, 337
Del Zanna L., Amato E., Bucciantini N., 2004, A&A, 421, 1063
Deshpande A. A., 2000, MNRAS, 317, 199
Draine B. T., 2011, Physics of the Interstellar and Intergalactic Medium
Faison M. D., Goss W. M., 2001, AJ, 121, 2706
Fryxell B., Olson K., Ricker P., Timmes F. X., Zingale M., Lamb D. Q., MacNeice P., Rosner R., Truran J. W., Tufo H., 2000, ApJS, 131, 273
Gaensler B. M., Jones D. H., Stappers B. W., 2002, ApJ, 580, L137
Gaensler B. M., Slane P. O., 2006, ARA&A, 44, 17
Gaensler B. M., van der Swaluw E., Camilo F., Kaspi V. M., Baganoff F. K., Yusef-Zadeh F., Manchester R. N., 2004, ApJ, 616, 383
Gotthelf E. V., 2004, in IAU Symposium, Vol. 218, Young Neutron Stars and Their Environments, Camilo F., Gaensler B. M., eds., p. 225
Hanke F., Marek A., Müller B., Janka H.-T., 2012, ApJ, 755, 138
Harrison P. A., Lyne A. G., Anderson B., 1993, MNRAS, 261, 113
Hobbs G., Lyne A. G., Kramer M., Martin C. E., Jordan C., 2004, MNRAS, 353, 1311
Jones D. H., Stappers B. W., Gaensler B. M., 2002, A&A, 389, L1
Kennel C. F., Coroniti F. V., 1984, ApJ, 283, 694
Komissarov S. S., Lyubarsky Y. E., 2004, MNRAS, 349, 779
Kulkarni S. R., Hester J. J., 1988, Nature, 335, 801
Manchester R. N., Hobbs G. B., Teoh A., Hobbs M., 2005, AJ, 129, 1993
Michel F. C., 1969, ApJ, 158, 727
Morlino G., Lyutikov M., Vorster M., 2015, MNRAS, 454, 3886
Noutsos A., Schnitzeler D. H. F. M., Keane E. F., Kramer M., Johnston S., 2013, MNRAS, 430, 2281
Patat F., Cox N. L. J., Parrent J., Branch D., 2010, A&A, 514, A78
Sagert I., Schaffner-Bielich J., 2008, A&A, 489, 281
Sutherland R. S., Dopita M. A., 1993, ApJS, 88, 253
Taylor J. H., Cordes J. M., 1993, ApJ, 411, 674
Tetzlaff N., Neuhäuser R., Hohle M. M., 2009, MNRAS, 400, L99
Toscano M., Sandhu J. S., Bailes M., Manchester R. N., Britton M. C., Kulkarni S. R., Anderson S. B., Stappers B. W., 1999, MNRAS, 307, 925
van Kerkwijk M. H., Ingle A., 2008, ApJ, 683, L159
van Kerkwijk M. H., Kulkarni S. R., 2001, A&A, 380, 221
Vigelius M., Melatos A., Chatterjee S., Gaensler B. M., Ghavamian P., 2007, MNRAS, 374, 793
Weisskopf M. C., Hester J. J., Tennant A. F., Elsner R. F., Schulz N. S., Marshall H. L., Karovska M., Nichols J. S., Swartz D. A., Kolodziejczak J. J., O'Dell S. L., 2000, ApJ, 536, L81
Wilkin F. P., 1996, ApJ, 459, L31
Yoon D., Morsony B., Heinz S., Wiersema K., Fender R. P., Russell D. M., Sunyaev R., 2011, ApJ, 742, 25